MULTIVARIATE TIME SERIES IMPUTATION WITH SIGNAL–NOISE DISENTANGLED GRAPH PROPAGATION

Anonymous authors
Paper under double-blind review

ABSTRACT

Missing data are pervasive in real-world multivariate time series, particularly in large-scale, high-frequency systems. Although recent graph-based and transformer-based methods achieve state-of-the-art (SOTA) performance by performing spatial graph propagation or leveraging self-attention mechanisms, they suffer from two key limitations: (1) treating each time series as an indivisible whole, without uncovering its internal temporal dynamics, and (2) relying on linear projections to connect spatial and temporal representations, which insufficiently depicts the complex spatial-temporal interactions. Motivated by the above limitations, we propose **GraphTSI**, a **Graph**-based multivariate **T**ime **S**eries **I**mputation method with signal-noise decomposition, where the signal component captures predictable dynamics and the noise component reflects unpredictable exogenous shocks of time series. To enable robust decomposition, we propose a prediction–subtraction framework where the prediction step progressively estimates predictable signal component, while the subtraction step uses the discrepancy between this estimate and the observed values to extract the exogenous noise component. Furthermore, for effective spatial-temporal interactions, we build an augmented bipartite graph that captures adaptive, non-linear transformation between spatial and temporal dimensions, and propagates signal and noise components through neighboring time series. Extensive experiments across nine datasets from three real-world domains demonstrate the superiority of GraphTSI, with average MAE improvements of 10.273% and 17.580% over graph-based and transformer-based SOTA methods, respectively.

1 INTRODUCTION

Multivariate time series data are among the most widespread data types in real-world applications, such as air quality monitoring (Yang et al., 2025a; Hoinaski et al., 2025), energy production or consumption regulating (Anonto et al., 2025; Jafarigorzin et al., 2025; Meha et al., 2025), and traffic analysis (Li et al., 2025; Gong et al., 2025). However, real-world time series are often incomplete due to equipment malfunctions, communication errors, or other data collection errors (Chen & Sun, 2021). The missing data prohibit downstream tasks like prediction (Wu et al., 2021; Zhou et al., 2022), classification (Wen et al., 2025), and data-driven analysis (Han et al., 2025; Wang et al., 2024) as they generally assume complete time series as inputs. To address this issue, multivariate time series imputation (Wang et al., 2025b) is studied to estimate missing values from observed data, ensuring the completeness of the time series for subsequent downstream applications.

In the literature, many works have been proposed for time series imputation. Early methods, such as weighted averaging and statistical models (Bashir & Wei, 2018; Moritz & Bartz-Beielstein, 2017), are used for imputation but fail to capture nonlinear patterns or long-term dependencies. Matrix factorization (LIU et al., 2023b; Yu et al., 2016; Chen et al., 2022) is employed to learn to fit on observed values with low-rank matrix multiplications to impute missing values, but their designs focus on in-sample fitting and lack temporal predictive capability. Generative methods (Yang et al., 2024; Islam et al., 2025) are also widely used to capture the data distribution for imputation, but suffer from training instability. Modern recurrent neural network (RNN)-based models (Che et al., 2018; Cao et al., 2018; Yoon et al., 2019) use gated mechanisms and hidden state propagation to capture intricate non-linear relationships for imputation, but iterative RNN is exceptionally time-consuming, and they usually struggle to leverage spatial interactions, making them prone to overfitting.

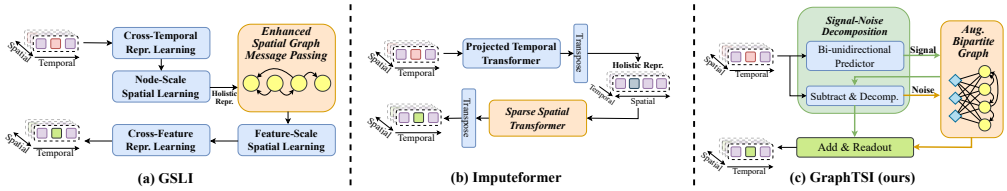

Figure 1: Structure comparison among GSLI, Imputeformer and GraphTSI

Recently, two promising imputation frameworks are emerging in the field: the graph-based methods (Yang et al., 2025b) and the transformer-based models (Nie et al., 2024). The graph-based models (overview in Figure 1(a)), with GSLI (Yang et al., 2025b) as representative, integrate spatial graph message passing layers to regularize information exchange. As for Transformer-based models (overview in Figure 1(b)), Imputeformer (Nie et al., 2024) stands out by incorporating a projected self-attention block and Fourier imputation loss to limit model expressivity against overfitting.

In spite of these breakthroughs, two critical limitations remain. The first is ***Insufficient Component Separation***. Multivariate time series can be represented as a composition of multiple components with distinct characteristics (Anderson, 2018; Cleveland & Cleveland, 1990). However, existing imputation methods treat each time series as a whole, directly imputing from observed inputs. While TIDER (LIU et al., 2023a) attempts to decompose time series into trend and seasonality components, it fails to capture interactions within noise, limiting its effectiveness. Moreover, time series decomposition is challenging in the presence of missing values. Conventional pre-processing decomposition commonly adopted in related fields (Zhou et al., 2022; Zeng et al., 2023; Wang et al., 2023) employs moving average or convolution, which exhibits large variance or even fails when long sequences of data are missing.

The second limitation is ***Linear Transformation of Spatial-Temporal Hidden States***. Spatial and temporal interactions differ in propagation and semantics (Yoon et al., 2019), making it essential to model them jointly yet distinctly for effective imputation. Existing methods follow the M-RNN (Yoon et al., 2019) structure, and stack interleaved spatial and temporal layers, via spatial graph message passing (Cini et al., 2021) and spatial attention (Nie et al., 2024), or employ spatial-temporal joint attention (Marisca et al., 2022; Wu et al., 2024). These methods forces the model to learn spatial and temporal representations that share the same feature space, leading to entangled or noisy features. Consequently, a key challenge lies in designing transformation layers that can effectively map between spatial and temporal representations, thereby capturing complex spatial-temporal interactions accurately.

Motivated by these limitations and the observation that a time series naturally exhibits two complementary components, with a signal component capturing predictable dynamics such as trend and seasonality, and a noise component reflecting unpredictable shocks, we propose GraphTSI, a **graph**-based **T**ime-**S**eries **I**mputation model with signal-noise decomposition (Figure 1c). The incomplete multivariate time series first passes through the *signal-noise decomposition block*, extracting signal and noise components. The two components further pass through the *augmented bipartite graph layer* to adaptively exchange spatial information, effectively capturing spatial-temporal interactions.

Specifically, for limitation 1, we propose a prediction-subtraction-based method for time series decomposition, grounded in the widely adopted data generation process (Anderson, 2018). It has two main steps: the prediction step and the subtraction step. With a new masked bi-unidirectional predictor, the prediction step actively predicts the signal component by utilizing either past or future information. This enforces signal prediction based on the learned temporal patterns rather than in-place filling, preventing information leakage from noise component. The subtraction step then compares the predicted signal component with the observed ground-truth to extract the noise component, thereby allowing separate and customized downstream processing of different components.

To address limitation 2, we construct an augmented bipartite graph in which structural spatial nodes and temporal nodes form two disjoint partitions, with spatial representations modeled as bipartite edges. To further regulate spatial interaction, we use augmented edges that directly connect pairs of spatial nodes within the spatial partition. Information is transmitted through three mechanisms: gather, propagate, and dispatch. The information is first gathered from the bipartite edges to derive spatial representations at each node. The introduced augmented edges facilitate direct information propagation among spatial nodes, effectively functioning as a spatial interaction layer. Finally, the

aggregated information is dispatched back onto the edges as updated temporal representations. This design enables flexible information exchange of spatial-temporal hidden states.

To sum up, our main contributions are as follows:

1. We propose a new method, GraphTSI, for multivariate time series imputation that integrates signal-noise decomposition with graph propagation.
2. We propose a prediction-subtraction-based method for decomposition via a masked bi-unidirectional prediction framework. It enables robust decomposition of signal components and noise components and remains effective even under extremely high missing rates.
3. We introduce an augmented bipartite graph for adaptive transformation between spatial and temporal representations, allowing more accurate component-specific feature interactions.
4. We conduct extensive experiments on 12 real-world multivariate time series datasets, achieving an average reduction in mean absolute error of 10.273% and 17.580% compared to GSLI and Imputeformer, respectively. Additional experiments on downstream tasks, ablation studies, extreme missing rates, robustness analysis, and case studies further solidify the effectiveness of our model.

2 PRELIMINARY

Notations and concepts. Consider a multivariate time series $\mathbf{X} \in \mathbb{R}^{N \times T \times C}$ comprising measurements from N distinguishable sensors observed over T time steps, where each sensor provides C channels of data. Specifically, the C-dimensional vector $\mathbf{X}_{i,t} \in \mathbb{R}^C$ from sensor i at time step t constitutes an ***observation***, where each scalar $\mathbf{X}_{i,t,c} \in \mathbb{R}$ denotes a ***measurement*** of channel c. Due to inevitable sensor failures in real-world deployments, completeness of observations is compromised. This is captured by a binary observation missing mask $\mathbf{M} \in \{0,1\}^{N \times T}$, where $\mathbf{M}_{i,t} = 0$ indicates a missing observation for sensor i at time step t.

To enhance imputation robustness against missing observations, we follow previous works (Nie et al., 2024; Cini et al., 2021) and incorporate two categories of exogenous information: (1) Temporal covariates $\mathbf{E}^{\mathrm{T}} \in \mathbb{R}^{T \times d_{\mathrm{T}}}$ such as time-of-day or day-of-week indices, representing cyclical patterns in measurements; (2) Spatial exogenous graph $\mathcal{G}^{\mathrm{S}} = \langle \mathcal{V}^{\mathrm{S}}, \mathcal{E}^{\mathrm{S}} \rangle$ with $\left|\mathcal{V}^{\mathrm{S}}\right| = N$, derived from geographical distances or naive correlation matrices, representing stationary spatial relationships among sensors. (implementation detail for each dataset is in Section B.1)

However, directly imputing over the full temporal horizon (especially for $T \gg 10^5$) is computationally prohibitive. To address this, we follow previous works (Yi et al., 2016; Cao et al., 2018; Cini et al., 2021; Nie et al., 2024) and adopt a sliding window approach by sampling subseries of length W ($W \ll T$) along the time axis. For a sliding window starting at time step t, we extract the following: (1) Ground truth $\mathbf{X}^{(t)} := \mathbf{X}_{:,t:t+W} \in \mathbb{R}^{N \times W \times C}$; (2) Missing mask $\mathbf{M}^{(t)} := \mathbf{M}_{:,t:t+W} \in \{0,1\}^{N \times W}$; (3) Partially observed input $\widetilde{\mathbf{X}}^{(t)} := \mathbf{M}^{(t)} \odot \mathbf{X}^{(t)}$, where $\odot$ denotes element-wise multiplication broadcasting over the channel dimension c; (4) Temporal covariates $\mathbf{E}^{\mathrm{T},(t)} := \mathbf{E}^{\mathrm{T}}_{t:t+W} \in \mathbb{R}^{W \times d_{\mathrm{T}}}$.

Problem Formulation. Given an incomplete multivariate time series $\widetilde{\mathbf{X}}^{(t)}$ and a missing mask $\mathbf{M}^{(t)}$, multivariate time series imputation aims to predict the unobserved entries in $\widetilde{\mathbf{X}}^{(t)}$ so that the imputed series $\widehat{\mathbf{X}}^{(t)}$ is as close as possible to the true series $\mathbf{X}^{(t)}$.

Data Generating Process. In the real world, the data generating process (DGP) of time series can vary widely across datasets and across time periods. We follow previous works (Blasques et al., 2020; Wu & Politis, 2024; Armillotta & Fokianos, 2023) and focus on two essential and complementary components commonly present in time series, signal and noise, to model the DGP. For each observation, we assume:

$$\mathbf{X}_{i,\tau} = f\left(\mathbf{X}_{:,<\tau}\right) + \varepsilon_{i,\tau} \tag{1}$$

where $f(\cdot)$ is a non-linear autoregressive function describing the predictable expected observation based on past information, which we refer to as the signal component. Conversely, $\mathrm{E}\left[\varepsilon_{i,\tau}\right] = 0$ corresponds to the exogenous noise component. Furthermore, related literature (Blasques et al., 2020; Wu & Politis, 2024; Armillotta & Fokianos, 2023) commonly adopts the following assumptions (see

Appendix A.3 for validity of these assumptions) regarding the statistical properties of $\varepsilon_{i,\tau}$:

$$\varepsilon_{i,\tau} \perp \mathbf{X}_{j,\omega}, \quad \forall j \in \{1, \ldots, N\}, \ \omega < \tau \tag{2}$$

$$\varepsilon_{i,\tau} \perp \varepsilon_{j,\omega}, \quad \forall j \in \{1, \ldots, N\}, \ \omega \neq \tau \tag{3}$$

$$\varepsilon_{i,\tau} \not\perp \varepsilon_{j,\tau}, \quad \forall j \in \{1, \ldots, N\} \tag{4}$$

The first assumption ensures each noise component to be independent of all prior observations. The second and third assumptions constrain the spatial-temporal interactions among noise components: those at different time steps are mutually independent, while contemporaneous ones may exhibit dependencies. In particular, noise at different time steps generally arises independently, whereas contemporaneous noise may arise from shared causes across variables, such as system-wide incidents or environmental disturbances.

3 Related Work

Extensive methods are proposed for multivariate time series imputation, and can be broadly categorized into the following paradigms: 1) *Statistical Methods*. Early methods were mainly statistical, using measures such as weighted averages, medians, modes, or linear interpolation (Moritz & Bartz-Beielstein, 2017; Bashir & Wei, 2018). 2) *Matrix Factorization Methods*. Matrix factorization approaches leverage the inherent low-rank and repetitive patterns in time series to estimate missing values through linear subspace modeling. For example, FGTI (Yu et al., 2016) incorporates high-frequency filtering to better exploit residual information, while LATC (Chen et al., 2022) introduces temporal regularization for improved local consistency. 3) *RNN-based Methods*. Representative RNN methods include GRU-D (Che et al., 2018), BRITS (Cao et al., 2018), M-RNN (Yoon et al., 2019), and NADE (Berglund et al., 2015), which leverage the recurrent structure to successively integrate information across time steps with hidden states in an auto-regressive paradigm. M-RNN (Yoon et al., 2019) introduces a interleaving temporal-spatial approach for imputation. BRITS (Cao et al., 2018) extends RNN with bidirectional inference and masked regression to better aggregate information from both past and future observations. 4) *Generative Methods*. Generative methods (Yang et al., 2024; Islam et al., 2025) are also widely used to capture the data distribution. 5) *Transformer-based Methods*. The transformer architecture (Vaswani et al., 2017) has demonstrated substantial performance gains in time series imputation by enabling global receptive fields via the self-attention mechanism. SAITS (Du et al., 2023) introduces a diagonally masked self-attention scheme. SPIN (Marisca et al., 2022) utilizes multiple sparse attention patterns to model intra-sensor and inter-sensor dependencies, which forces all states to share the same representation space, hindering preformance. Imputeformer (Nie et al., 2024) exploits the low-rank structure of time series by employing projected temporal attention and spatial embedding attention. 6) *Graph-based Methods*. Graph-based approaches model multivariate time series imputation as a node or edge feature completion task on spatial graphs, where sensors are represented as nodes, and relationships as edges. For instance, STCAGCN (Nie et al., 2023) focuses on traffic data and dynamically constructs graphs based on additional speed sensor information. FC-GNN (Satorras et al., 2022) leverages spatial graph to capture intra-sensor dependencies. GACN (Ye et al., 2021) employs graph convolution layers to refine spatial encoding. STAR (Liang et al., 2023) merges temporal features into spatial features for node propagation. GRIN (Cini et al., 2021) integrates GRU to iteratively aggregate temporal information with spatial message passing for spatial-temporal fusion. GSLI (Yang et al., 2025b) introduces multi-scale graph structure learning to enhance spatial correlations. Graph-based methods are also widely used in tabular data (Wang et al., 2025a).

4 Methods

The overview of GraphTSI is shown in Figure 2. Specifically, given an incomplete multivariate time series, GraphTSI first maps observations into information-rich vectors via the missing-aware input embedding (Section 4.1). Inside the signal-noise decomposition block (Section 4.2), a bi-unidirectional predictor estimates univariate signals from these embeddings, followed by an augmented bipartite graph (Section 4.3) for spatial interactions, yielding the updated signal components. Then, signal and noise components are separated by subtracting the predicted signal from observed ground truth, followed by an augmented bipartite graph for missing noise imputation. Finally, imputation is generated via MLP readout of aggregated signal and noise components.

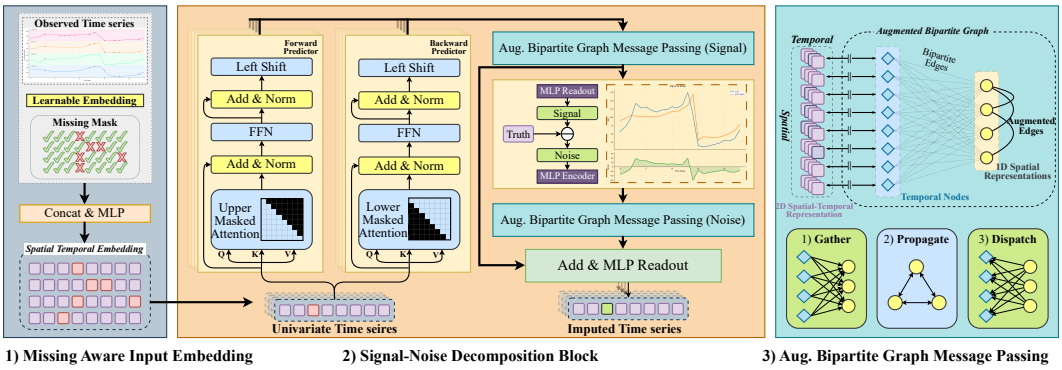

Figure 2: The architecture overview of the model.

4.1 Missing Aware Input Embedding

Conventional embedding methods typically employ an MLP for feature extraction and concatenate temporal positional embedding afterwards. However, this approach fails to differentiate between missing and observed measurements. Therefore, we adapt from (Lipton et al., 2016) and use missing-aware input embedding through concatenating temporal positions, missing masks and observed ground truth prior the MLP. Formally, given $\widetilde{\mathbf{X}}^{(t)}$, $\mathbf{M}^{(t)}$ and $\mathbf{E}^{\mathrm{T},(t)}$:

$$\mathbf{h}_{i,\tau}^{(0)} = \mathrm{MLP}\left(\widetilde{\mathbf{X}}_{i,\tau}^{(t)} \middle\| \mathbf{M}_{i,\tau}^{(t)} \middle\| \mathbf{E}_{i,\tau}^{\mathrm{T},(t)}\right) \tag{5}$$

where $i \in [1, N]$ indexes the sensors and $\tau \in [1, W]$ indexes the time steps. As for the exogenous temporal covariates, we followed previous works (Vaswani et al., 2017; Nie et al., 2024) with a sinusoidal time-of-day encoding for each observation.

4.2 Signal-Noise Decomposition

To decompose signal and noise in time series data, we propose a prediction-subtraction method that first predicts the predictable signal component from past observations and then subtracts the signal component from the observed ground truth to extract the noise component. Theorem 2 shows that training on raw observations is equivalent to training on their predictable signal, ensuring that the predictor captures the signal without being affected by noise, and thus validating our prediction–subtraction-based approach.

Bi-unidirectional Prediction Step. We adopt a bi-unidirectional design with two independent unidirectional predictors in opposite directions. This approach preserves identifiability between signal and noise while enhancing boundary prediction through aggregating complementary evidence from both directions. For clarity, we will describe only the forward unidirectional predictor; the reverse direction is implemented analogously.

The forward predictor estimates the expected univariate signal component for each sensor over the time axis. We adopt a standard Transformer (Vaswani et al., 2017) as the backbone due to its parallelization efficiency and simplicity. Specifically, we apply a triangularly masked self-attention mechanism across the temporal dimension:

$$\begin{aligned} \mathbf{h}_i^{(l),\mathrm{attn,f}} &= \mathrm{MaskedSelfAttn}\left(\mathbf{h}_i^{(l-1)}, \mathbf{h}_i^{(l-1)}, \mathbf{h}_i^{(l-1)}\right) \\ &= \mathrm{MaskedSoftmax}\left(\frac{\mathbf{h}_i^{(l-1)}\mathbf{W}_Q\mathbf{W}_K^{\top}\mathbf{h}_i^{(l-1),\top}}{\sqrt{d_{\mathrm{h}}}}\right)\mathbf{h}_i^{(l-1)}\mathbf{W}_V \end{aligned} \tag{6}$$

where $\mathbf{W}_Q, \mathbf{W}_K, \mathbf{W}_V \in \mathbb{R}^{\mathrm{d}_h \times \mathrm{d}_h}$ are learnable projection matrices, and $\mathrm{MaskSoftmax}(\cdot)$ applies an upper-triangular masking so that each time step only attend to previous and current observations. The resulting hidden states then pass through residually connected layer normalization and feed

forward layers to increase expressivity:

$$\mathbf{h}_i^{(l),\mathrm{norm,f}} = \mathrm{LayerNorm}\left(\mathbf{h}_i^{(l-1)} + \mathbf{h}_i^{(l),\mathrm{attn,f}}\right) \tag{7}$$

$$\mathbf{h}_i^{(l),\mathrm{ffn,f}} = \mathrm{LayerNorm}\left(\mathbf{h}_i^{(l),\mathrm{norm,f}} + \mathrm{FFN}\left(\mathbf{h}_i^{(l),\mathrm{norm,f}}\right)\right) \tag{8}$$

However, residual connections and triangular self-attention allow present-step information to leak into each hidden state, potentially causing trivial auto-encoding solutions. To ensure that hidden states only incorporates historical information, we shift the features one step forward in time:

$$\widetilde{\mathbf{h}}_{i,:}^{(l),\mathrm{signal,f}} = \mathbf{W}_{\mathrm{fill,f}} \Big\| \mathbf{h}_{i,1:W}^{(l),\mathrm{ffn,f}} \tag{9}$$

where $\mathbf{W}_{\mathrm{fill,f}} \in \mathbb{R}^{N \times \mathrm{d}_h}$ is a learnable hidden state for the first time step.

Augmented Bipartite Graph for Signal. This signal hidden state only contains univariate information within each time series, so we pass them through the augmented bipartite graph transformation for spatial interactions and retrieve the full multivariate signal features: $\mathbf{h}_{i,:}^{(l),\mathrm{signal,f}} = \mathrm{AugBipGraph}_{\mathrm{signal}}\left(\widetilde{\mathbf{h}}_{i,:}^{(l),\mathrm{signal,f}}\right)$, where $\mathrm{AugBipGraph}_{\mathrm{signal}}(\cdot)$ represents the customized signal augmented bipartite graph in Section 4.3.2.

Subtraction Step. To separate the two components, we first extract our predicted signal component from information-rich hidden state through an MLP readout: $\widehat{\mathbf{X}}_{i,\tau}^{(l),\mathrm{signal,f}} = \mathrm{MLP}\left(\mathbf{h}_{i,\tau}^{(l),\mathrm{signal,f}}\right)$. Subsequently, the exogenous noise component is extracted from observed measurements by subtracting the predicted signal from observed ground truth:

$$\widetilde{\mathbf{X}}_{i,\tau}^{(l),\mathrm{noise,f}} = \mathbf{M}_{i,\tau}^{(t)} \times \left(\widetilde{\mathbf{X}}_{i,\tau}^{(t)} - \widehat{\mathbf{X}}_{i,\tau}^{(l),\mathrm{signal,f}}\right) \tag{10}$$

Missing entries where $\mathbf{M}_{i,\tau}^{(t)} = 0$ are set to 0. Now, extracted noise component in both directions are concatenated and passes through another missing-aware embedding to produce complete noise features for downstream imputation: $\widetilde{\mathbf{h}}_{i,\tau}^{(l),\mathrm{noise}} = \mathrm{MLP}\left(\widetilde{\mathbf{X}}_{i,\tau}^{(l),\mathrm{noise,f}} \Big\| \widetilde{\mathbf{X}}_{i,\tau}^{(l),\mathrm{noise,b}} \Big\| \mathbf{M}_{i,\tau}^{(t)}\right)$. Here, $\widetilde{\mathbf{h}}_{i,\tau}^{(l),\mathrm{noise}}$ is the initial noise embedding and acts as the input for imputing the missing noise components through the augmented bipartite graph.

4.3 Augmented Bipartite Graph Transformation

We construct an augmented bipartite graph to capture both spatial-temporal representation transformation and spatial dependencies among sensors. The graph consists of two types of nodes: temporal nodes and spatial nodes, with bipartite edges in between to form a bipartite structure and additional augmented edges for spatial information propagation. Formally, the bipartite graph is defined as: $\mathcal{G}^{\mathrm{bip}} = \left\langle \mathcal{V}^{\mathrm{T}} \bigcup \mathcal{V}^{\mathrm{S}}, \mathcal{E}^{\mathrm{bip}} \right\rangle$, where $\mathcal{V}^{\mathrm{T}} = \{v_1^t, \ldots, v_W^t\}$ denotes the set of temporal nodes; $\mathcal{V}^{\mathrm{S}} = \{v_1^s, \ldots, v_N^s\}$ the set of spatial nodes; and $\mathcal{E}^{\mathrm{bip}} = \{(v_i^{\mathrm{t}}, v_\tau^{\mathrm{s}}) | \mathbf{M}_{i,\tau}^{(t)} = 1\}$ the set of bipartite edges, corresponding to each spatial-temporal observations. In addition, we introduce the spatial exogenous graph $\mathcal{G}^{\mathrm{S}} = \langle \mathcal{V}^{\mathrm{S}}, \mathcal{E}^{\mathrm{S}} \rangle$ connecting pairs of spatial nodes as the augmented propagation graph. The initial representations $\widetilde{\mathbf{h}}_{i,\tau}^{(l),\mathrm{signal}}$ or $\widetilde{\mathbf{h}}_{i,\tau}^{(l),\mathrm{noise}}$ computed for signal components and noise components respectively are naturally mapped to the edge embedding of corresponding bipartite edges $(v_i^{\mathrm{t}}, v_\tau^{\mathrm{s}})$, such that each edge embeds all relevant information associated with observation $\mathbf{X}_{i,\tau}^{(t)}$. This construction allows the model to flexibly convert temporal and spatial representation via edge-node message propagation within $\mathcal{G}^{\mathrm{bip}}$, and present spatial interactions through node-node message propagation within $\mathcal{G}^{\mathrm{S}}$. We first introduce a generalized message passing procedure on the augmented graph, which can be customized for signal and noise to better fit their characteristics.

4.3.1 Generalized Message Passing Procedure

The proposed message passing framework consists of three mechanisms: 1) ***Gather***; 2) ***Propagate***; 3) ***Dispatch***. These three mechanisms transform temporal presentation to spatial representation, exchange spatial information and transform them back to temporal representations. Specifically:

Gather. For each spatial node i, the gather function aggregates temporal representations from bipartite edges associated with sensor i to form a spatial representation:

$$\mathbf{h}_i^{(l),\text{gather}} = \text{Gather}\left(\left\{\widetilde{\mathbf{z}}_{i,\tau}^{(l)} \middle| (v_i^{\text{t}}, v_\tau^{\text{s}}) \in \mathcal{E}^{\text{bip}}\right\}\right) \tag{11}$$

where $\widetilde{\mathbf{z}}_{i,\tau}^{(l)}$ is the input bipartite edge embedding (i.e. $\widetilde{\mathbf{h}}_{i,\tau}^{(l),\text{signal}}$ for signal and $\widetilde{\mathbf{h}}_{i,\tau}^{(l),\text{noise}}$ for noise).

Propagate. Spatial nodes propagate information the spatial exogenous graph $\mathcal{G}^{\text{S}}$:

$$\mathbf{h}_i^{(l),\text{prop}} = \text{FFN}\left(\sum_{j \in \text{N}(i;\mathcal{E}^{\text{S}})} \mathbf{W}_{i,j} \mathbf{h}_i^{(l),\text{gather}}\right) \tag{12}$$

where $\text{N}\left(i; \mathcal{E}^{\text{S}}\right)$ denotes all neighbors of node v_i^{s} connected via the given spatial exogenous graph edge set $\mathcal{E}^{\text{S}}$; $\mathbf{W}_{i,j}$ specifies the learnable edge weight for that spatial graph, allowing signal and noise to share the same graph structure, but adopt independent relationships through learnable parameters. To provide this flexibility, we utilize a learnable characteristic matrix $\mathbf{E}^{\text{S}} \in \mathbb{R}^{N \times d_{\text{S}}}$, and compute the edge weights as: $\mathbf{W} = \text{Softmax}\left(\mathbf{E}^{\text{S}} \mathbf{W}^{(l)} \mathbf{E}^{\text{S},\top}, \text{dim} = 1\right)$, where $\mathbf{W}^{(l)} \in \mathbb{R}^{d_{\text{S}} \times d_{\text{S}}}$ is a component-specific projection matrix for signal and noise.

Dispatch. The updated spatial node representations are distributed back to bipartite graph edges as temporal representations for inference: $\mathbf{z}_{i,\tau}^{(l)} = \text{Dispatch}\left(\mathbf{h}_i^{(l),\text{prop}}\right)$ where $\mathbf{z}_{i,\tau}^{(l)}$ is the updated temporal representation ($\mathbf{h}_{i,\tau}^{(l),\text{signal}}$ for signal and $\mathbf{h}_{i,\tau}^{(l),\text{noise}}$ for noise).

Readout. Finally, we form a combined representation by concatenating both updated signal features with the updated noise features, from which an MLP readout yields the final imputation: $\widehat{\mathbf{X}}_{i,\tau}^{(t)} = \text{MLP}\left(\mathbf{h}_{i,\tau}^{(l),\text{signal,f}} \middle\| \mathbf{h}_{i,\tau}^{(l),\text{signal,b}} \middle\| \mathbf{h}_{i,\tau}^{(l),\text{noise}}\right)$

The training objective of GraphTSI follows previous works (Du et al., 2023), combining both the observed reconstruction loss and the masked imputation loss (see Section B.3 for more details).

4.3.2 Customization for Signal and Noise Components

Customization for Signal Components. Signal components tend to exhibit temporal redundancy with smooth transitions (Nie et al., 2024). To capture these properties, we employ a projected attention for the gather and dispatch functions:

$$\text{Gather}_{\text{signal}}\left(\left\{\widetilde{\mathbf{h}}_{i,\tau}^{(l),\text{signal}} \middle| (v_i^{\text{t}}, v_\tau^{\text{s}}) \in \mathcal{E}^{\text{bip}}\right\}\right) = \text{Flatten}\left(\text{Attn}\left(\mathbf{W}_{\text{proj}}, \mathbf{h}_{i,:}^{(l),\text{shift}}, \widetilde{\mathbf{h}}_{i,\tau}^{(l),\text{signal}}\right)\right) \tag{13}$$

where $\text{Attn}(\cdot)$ denotes the standard attention mechanism from (Vaswani et al., 2017); while $\mathbf{W}_{\text{proj}} \in \mathbb{R}^{H \times d_{\text{h}}}$ is the learnable query matrix that projects the original W time steps to H ($H \ll W$) heads in the latent space; and $\text{Flatten}(\cdot) : \mathbb{R}^{H \times d_{\text{h}}} \mapsto \mathbb{R}^{H d_{\text{h}}}$ stacks all heads into a single high dimensional vector as the spatial representation. Similarly, to recover signal features during dispatch, we perform the reverse process: un-flatten the updated spatial representations, then apply an attention to project them back to temporal representations for each time step:

$$\text{Dispatch}_{\text{signal}}\left(\mathbf{h}_i^{(l),\text{signal,prop}}\right) = \text{Attn}\left(\widetilde{\mathbf{h}}_{i,\tau}^{(l),\text{signal}}, \mathbf{W}_{\text{proj}}, \text{Unflatten}\left(\mathbf{h}_i^{(l),\text{signal,prop}}\right)\right) \tag{14}$$

where $\text{Unflatten}(\cdot) : \mathbb{R}^{H d_{\text{h}}} \mapsto \mathbb{R}^{H \times d_{\text{h}}}$ is the inverse of flatten. This encoder-decoder structure enables compact latent encoding and robust signal recovery, thereby reducing noise and increasing computational efficiency specifically for signal components.

Customization for Noise Components. Noise components capture sudden, non-repetitive features, with little temporal redundancy among the inputs. Therefore, we preserve all information by performing direct flatten and un-flatten operations without additional processing. Formally:

$$\text{Gather}_{\text{noise}}\left(\left\{\widetilde{\mathbf{h}}_{i,\tau}^{(l),\text{noise}} \middle| (v_i^{\text{t}}, v_\tau^{\text{s}}) \in \mathcal{E}^{\text{bip}}\right\}\right) = \text{Flatten}\left(\widetilde{\mathbf{h}}_{i,\tau}^{(l),\text{noise}}\right) \tag{15}$$

$$\text{Dispatch}_{\text{noise}}\left(\mathbf{h}_i^{(l),\text{noise,prop}}\right) = \text{Unflatten}\left(\mathbf{h}_i^{(l),\text{noise,prop}}\right) \tag{16}$$

where $\text{Flatten}(\cdot) : \mathbb{R}^{W \times d_{\text{h}}} \mapsto \mathbb{R}^{W d_{\text{h}}}$ and $\text{Unflatten}(\cdot) : \mathbb{R}^{W d_{\text{h}}} \mapsto \mathbb{R}^{W \times d_{\text{h}}}$ act as dimension-preserving transformations for maximal retention of abrupt exogenous noise event information.

4.4 Analysis

Superiority of GraphTSI. In Theorem 1, we show that conventional spatial-temporal interconversion and interaction layers arise as special cases of our framework. The proof is in Section A.2.

Theorem 1. *The spatial-temporal information exchange mechanism employed by existing state-of-the-art multivariate imputation methods (i.e., GRIN, GSLI, and Imputeformer) can be regarded as a special case of our proposed method.*

Time Complexities Analysis. The missing aware input embedding has a time complexity of $O(WNCd_{\mathrm{h}})$. The bi-unidirectional predictors adopt standard transformer architecture, leading to a time complexity of $O(W^2Nd_{\mathrm{h}})$. The augmented bipartite graph gathers and dispatches information with a time complexity of $O(WHNd_{\mathrm{h}})$ for signal and $O(WNd_{\mathrm{h}})$ for noise component. Propagation is $O(\left|\mathcal{E}^{\mathrm{S}}\right| Hd_{\mathrm{h}})$ for signal and $O(\left|\mathcal{E}^{\mathrm{S}}\right| Nd_{\mathrm{h}})$ for noise, where H is the number of latent heads, and $\left|\mathcal{E}^{\mathrm{S}}\right|$ is the number of edges in exgenous spatial graph. The overall time complexity is $O\left(WNd_{\mathrm{h}}\left(W+H+C\right)+\left|\mathcal{E}^{\mathrm{S}}\right| d_{\mathrm{h}}(H+N)\right)$, which scales quadratically with window sizes. Additional results on model efficiency can be found in Figure 6.

5 Experiments

5.1 Experimental Setup

Datasets. Following previous works (Nie et al., 2024; Cini et al., 2021), we use 9 real-world public datasets, including AQI36, AQI, METR-LA, PEMS-BAY, PEMS03, PEMS04, PEMS07, PEMS08, and HAR (Details in Section B.1). We adopt MAE and RMSE as evaluation metrics, with their definitions and the dataset masking strategy detailed in Section B.2.

Baselines. We compare GraphTSI with nine baselines spanning various categories: (1) **Average**: Statistical average of each sensor; (2) **GRIN** (Cini et al., 2021): A graph-based model combining GRU with message passing for imputation; (3) **GSLI** (Yang et al., 2025b): A graph-based model with multi-scale graph structure learning for imputation; (4) **BRITS** (Cao et al., 2018): A bidirectional RNN model for imputation; (5) **TIDER** (LIU et al., 2023a): A matrix factorization method with explicit modeling for different time series components; (6) **adaTIDER** (Liu et al.): A matrix factorization method that incorporates adaptive cross-channel dependency modeling and multi-period seasonality representations; (7); **LCR** (Chen et al.): An efficient low-rank Laplacian convolutional representation model. (8) **UnIMP** (Wang et al., 2025a): A SOTA tabular imputation method; (9) **SAITS** (Du et al., 2023): A transformer-based model with diagonally masked attention blocks; (10) **Imputeformer** (Nie et al., 2024): A low-rank induced transformer-based model.

Implementation Details. We follow Imputeformer (Nie et al., 2024) for experimental settings, with a default point missing rate of 25%, block missing rate of 0.5%, and window size of 24. The model is trained for a maximum of 300 epochs with patience of 30. All tests are done with seed 2. Experiments are conducted on a server equipped with a 24 GB NVIDIA RTX 4090 GPU.

5.2 Results

Overall Results. We evaluate imputation error across all datasets, with MAE results shown in Table 1, and RMSE results shown in Table 3. As we can see, the transformer-based SOTA Imputeformer performs well in traffic and HAR datasets, where time series exhibit strong seasonal repetition, but performs poorly when such seasonality is absent. Graph-based SOTA GSLI performs well on PEMS datasets with multiple channels per sensor. Our GraphTSI, with signal-noise decomposition design and augmented bipartite graph, performs best in all scenarios, achieving an average MAE improvement of 17.215% over Imputeformer and 9.557% over GSLI, respectively.

Ablation Study. This experiment conducts an ablation study on key components of GraphTSI. Specifically, we consider three ablation setups: 1) ***w/o Noise***: We remove the Signal-Noise decomposition layer and directly decode results from signal features $\mathbf{h}_{i,:}^{(l),\mathrm{signal,f}}$ and $\mathbf{h}_{i,:}^{(l),\mathrm{signal,b}}$; 2) ***Bidirectional***: We employ a bidirectional approach instead of the bi-unidirectional approach for the prediction step; 3) ***w/o Graph***: We disable spatial interactions for augmented bipartite graph message passing by setting the adjacency matrix to a unit matrix. Ablations are performed on AQI, PEMS08, and HAR to maximize domain diversity. Results summarized in Figure 3 indicate that the three techniques bring an average performance gain of 15.648%, 5.561%, and 43.788%, respectively.

Dataset	Mask	Avg.	GRIN	GSLI	BRITS	TIDER	adaTIDER	LCR	UnIMP	SAITS	Imputeformer	GraphTSI	
AQI36	Simulated	52.6813	12.5883	12.8262	14.1221	24.2235	47.7634	54.7605	19.4776	16.3931	13.9852	**10.3630**	**-17.678%**
AQI		39.8759	14.7626	15.8241	19.8495	32.7432	31.9666	33.3918	21.1230	21.6905	16.3739	**13.2298**	**-10.383%**
METR-LA	Point	15.0783	1.8863	1.7012	3.7869	9.2683	10.1894	9.5630	2.2684	3.0864	1.6891	**1.6339**	**-3.268%**
	Block	15.1521	2.5720	2.3399	3.9786	9.6889	10.9506	9.3800	3.3800	3.7550	2.3017	**2.2353**	**-2.885%**
PEMS-BAY	Point	5.3772	0.6570	0.6167	1.9095	3.9580	4.0253	4.2214	0.8945	1.6308	0.5870	**0.5692**	**-1.980%**
	Block	5.4192	1.0668	1.0749	1.9474	3.9384	3.9962	4.1967	1.4736	1.9188	1.0253	**0.9473**	**-7.608%**
PEMS03	Point	85.2738	9.2689	7.6272	12.6884	34.4900	37.5310	36.4490	11.1235	15.2878	7.4442	**7.0871**	**-4.797%**
	Block	85.8496	11.6494	9.1688	12.2455	31.8528	41.1549	33.0797	15.4294	15.4563	8.8392	**8.1013**	**-8.348%**
PEMS04	Point	36.4437	5.4738	2.6111	6.7712	15.2647	16.3088	15.2068	6.0129	8.1783	5.6620	**2.5512**	**-2.294%**
	Block	36.6491	7.9954	5.0697	7.4038	15.0324	15.6130	15.2393	7.0645	8.4292	6.3202	**4.5507**	**-10.237%**
PEMS07	Point	121.8156	11.7727	10.1087	23.9394	53.4188	54.5748	46.5116	16.7349	27.4032	10.6516	**10.0745**	**-0.338%**
	Block	122.3093	14.7600	13.1901	23.7428	51.2491	54.3342	46.7072	20.0892	28.2561	13.8238	**12.7600**	**-3.261%**
PEMS08	Point	31.1824	4.2496	1.9014	5.5024	13.5194	15.0606	12.6943	4.5164	6.8455	4.0626	**1.8007**	**-5.296%**
	Block	31.3436	7.0010	4.1167	5.9880	13.2764	14.7039	12.5099	6.5420	7.3250	4.6939	**3.6018**	**-12.508%**
HAR	Point	0.2327	D.N.F.	0.0276	0.0481	0.1584	0.1288	0.1712	0.0640	0.0545	0.0283	**0.0249**	**-9.619%**
	Block	0.2284	D.N.F.	0.0325	0.0380	0.1219	0.0722	0.1259	0.1660	0.0516	0.0277	**0.0237**	**-14.440%**
ETTm1	Point	5.9672	0.7907	0.4685	0.5749	2.6206	2.1944	3.2588	D.N.F.	0.4805	0.4779	**0.4469**	**-4.610%**
	Block	3.6908	D.N.F.	0.4991	0.5822	2.5922	2.1853	3.2951	D.N.F.	0.4483	0.5763	**0.4179**	**-6.781%**
ETTm2	Point	6.4075	D.N.F.	0.3539	0.8668	4.1097	3.2316	5.3046	D.N.F.	0.3869	0.3956	**0.2752**	**-22.238%**
	Block	6.3221	D.N.F.	0.8787	1.4765	4.1759	3.1788	5.2098	D.N.F.	0.8460	1.2310	**0.7001**	**-17.246%**
Elergone	Point	244.1358	D.N.F.	27.3681	85.3951	155.5574	158.5652	165.6583	34.9038	72.5428	27.7954	**27.2700**	**-0.358%**
	Block	241.0613	D.N.F.	44.7311	82.2766	147.5384	150.2892	154.7714	67.3998	68.9966	41.3560	**40.5752**	**-1.888%**
Average Improvement		**-88.050%**	**-27.147%**	**-10.273%**	**-47.648%**	**-78.350%**	**-79.477%**	**-80.247%**	**-44.039%**	**-45.890%**	**-17.580%**	—	

Table 1: MAE results. The final column shows average gain over second best method, and the final row shows average gain over each model. D.N.F. indicates not finished within 8 hours for ETTm1, ETTm2 and Elergone datasets and not finished within 48 hours for other datasets.

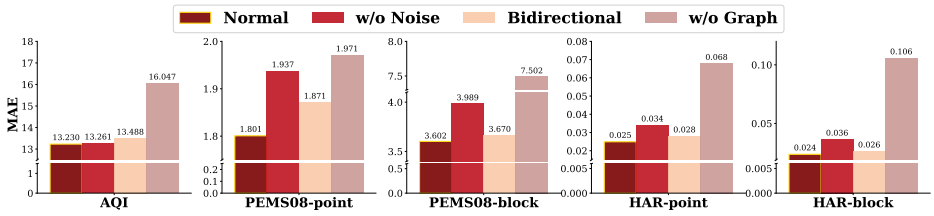

Figure 3: Ablation study on different datasets

Downstream Task. In this experiment, we evaluate the downstream classification performance on the HAR dataset. We employ a simple MLP layer as our classifier for all models, including results from ground-truth datasets (with no missing observations). Figure 4(a) presents the classification results. This shows that improved imputation quality can improve downstream task accuracy, with GraphTSI being outperforming other models both in point missing and block missing scenarios.

Different Missing Rates. We compare the performance of GraphTSI against SOTA models, including Imputeformer and GSLI, under various missing rates in Figure 4(b). More results are in Section C.2. Generally, performance degrades for all models under extremely sparse data. GraphTSI degrades slower compared to other models. Specifically, GraphTSI achieves 4.597% and 83.197% improvement over GSLI and Imputeformer, respectively, when the missing rate is 95%.

Hyperparameter Analysis. We investigate two hyperparameters: window size W and model layers L. Results are shown in Figure 4(c) and Figure 4(d), respectively. More results are in Section C.3. As shown, GraphTSI produces stable imputation results across window sizes and model layers.

Case Studies. We demonstrate model explainability using intermediate results on the AQI36 dataset. Figure 5(a) presents visualization for the decomposed signal, noise, and model imputation. In the imputed region, sensors 4 and 13 exhibit similar downward signal components, while noise components show high variability. This separation demonstrates GraphTSI's capability to model the

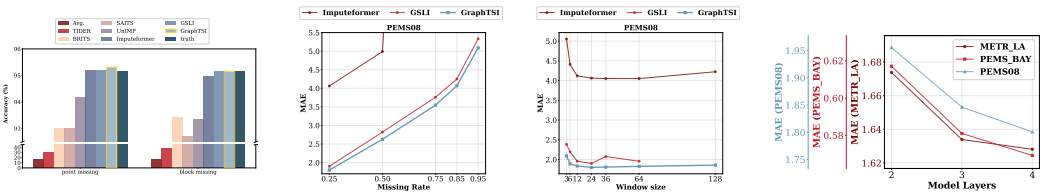

(a) Downstream (b) Missing rate (c) Window size (d) Model layer

Figure 4: Results of downstream classification, different missing rates and hyper-parameters.

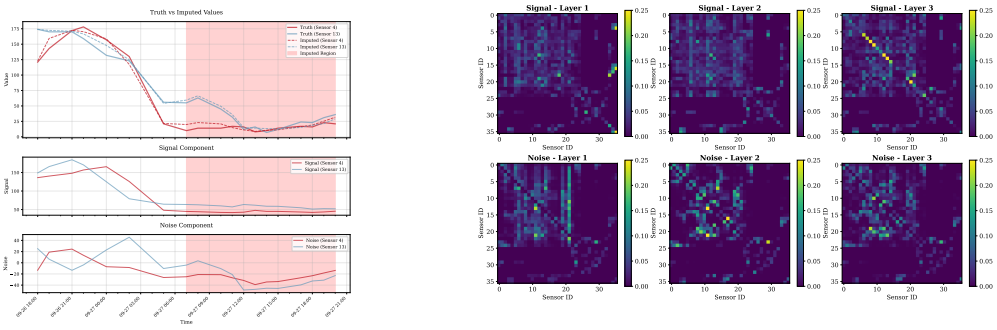

(a) Decomposed signal-noise

(b) Adjacency matrix

Figure 5: Case Study of Decomposed Signal-Noise and Adjacency Matrix.

distinct spatial interaction of signal and noise components with component-specific adjacency matrices. Further evidence (Figure 5(b)) visualizes learned adjacency weights of the augmented bipartite graph, where we can see distinct relationships in the upper-left corner: Signal components show two densely connected sub-regions, whereas noise interactions reveal complex sensor relationships.

Model Efficiency. In this experiment, we report the average inference speed and imputation error of different models to compare the efficiency of our model against other methods. Results are shown in Figure 6. Relative MAE is defined as the ratio between a model's MAE and the lowest MAE achieved by any model on the same dataset. On all the datasets, GraphTSI steadily delivers best imputation performance while maintaining inference speeds comparable to other strong baselines.

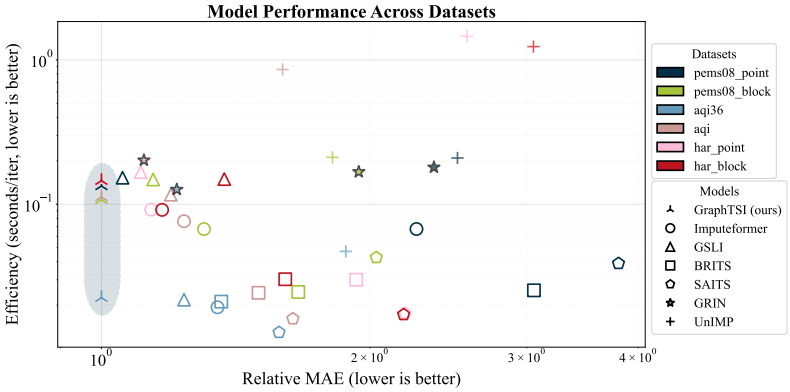

Figure 6: Average inference time and relative imputation error of different models.

6 Conclusion

In this paper, we propose GraphTSI, a graph-based multivariate time series imputation method. By leveraging a prediction–subtraction framework that decomposes each series into predictable signals and exogenous noise, and propagating information through an augmented bipartite graph for adaptive spatial–temporal representation, GraphTSI effectively captures essential information for accurate imputation. Experiments on 9 real-world datasets show the consistent superiority of GraphTSI.

7 Reproducibility Statement

We have taken multiple steps to facilitate reproducibility. Implementation details, including default missing rates, window sizes, training epochs, and training seed are documented in Section 5.1. We release anonymized code, scripts and configuration files for training, evaluating, as well as reproducing all reported tables at the following anonymous repository: https://anonymous.4open.science/r/timeseries-imputation-2E5B/README.md. Specific dataset usage and pre-processing steps are disclosed in Appendix B.1 and Appendix B.2.

References

O. D. Anderson. Time-series. 25(4):308–310, 2018. ISSN 2515-7884. doi: 10.2307/2988091. URL https://doi.org/10.2307/2988091. _eprint: https://academic.oup.com/jrsssd/article-pdf/25/4/308/49917313/jrsssd_25_4_308a.pdf.

Hasanur Zaman Anonto, Md Ismail Hossain, Abu Shufian, Protik Parvez Sheikh, Sadman Shahriar Alam, Md. Shaoran Sayem, and S M Tanvir Hassan Shovon. Analyzing energy consumption trends and environmental influences: A time-series study on temperature, renewables, and demand correlations. *Cleaner Energy Systems*, 12:100209, 2025. ISSN 2772-7831. doi: https://doi.org/10.1016/j.cles.2025.100209. URL https://www.sciencedirect.com/science/article/pii/S2772783125000408.

Mirko Armillotta and Konstantinos Fokianos. Nonlinear network autoregression. *The Annals of Statistics*, 51(6):2526–2552, 2023.

Faraj Bashir and Hua-Liang Wei. Handling missing data in multivariate time series using a vector autoregressive model-imputation (var-im) algorithm. *Neurocomputing*, 276:23–30, 2018. ISSN 0925-2312. doi: https://doi.org/10.1016/j.neucom.2017.03.097. URL https://www.sciencedirect.com/science/article/pii/S0925231217315515. Machine Learning and Data Mining Techniques for Medical Complex Data Analysis.

Mathias Berglund, Tapani Raiko, Mikko Honkala, Leo Kärkkäinen, Akos Vetek, and Juha T Karhunen. Bidirectional recurrent neural networks as generative models. *Advances in neural information processing systems*, 28, 2015.

Francisco Blasques, Siem Jan Koopman, and André Lucas. Nonlinear autoregressive models with optimality properties. *Econometric Reviews*, 39(6):559–578, 2020.

Wei Cao, Dong Wang, Jian Li, Hao Zhou, Lei Li, and Yitan Li. Brits: Bidirectional recurrent imputation for time series. *Advances in neural information processing systems*, 31, 2018.

Zhengping Che, Sanjay Purushotham, Kyunghyun Cho, David Sontag, and Yan Liu. Recurrent neural networks for multivariate time series with missing values. 8(1):6085, 2018. ISSN 2045-2322. doi: 10.1038/s41598-018-24271-9. URL https://www.nature.com/articles/s41598-018-24271-9. Publisher: Nature Publishing Group.

Xinyu Chen and Lijun Sun. Bayesian temporal factorization for multidimensional time series prediction. *IEEE Transactions on Pattern Analysis and Machine Intelligence*, pp. 1–1, 2021. ISSN 1939-3539. doi: 10.1109/tpami.2021.3066551. URL http://dx.doi.org/10.1109/TPAMI.2021.3066551.

Xinyu Chen, Zhanhong Cheng, HanQin Cai, Nicolas Saunier, and Lijun Sun. Laplacian convolutional representation for traffic time series imputation. 36(11):6490–6502. ISSN 1558-2191. doi: 10.1109/TKDE.2024.3419698. URL https://ieeexplore.ieee.org/document/10574327.

Xinyu Chen, Mengying Lei, Nicolas Saunier, and Lijun Sun. Low-rank autoregressive tensor completion for spatiotemporal traffic data imputation. *IEEE Transactions on Intelligent Transportation Systems*, 23(8):12301–12310, 2022. doi: 10.1109/TITS.2021.3113608.

Andrea Cini, Ivan Marisca, and Cesare Alippi. Filling the g_ap_s: Multivariate time series imputation by graph neural networks. In *International Conference on Learning Representations*, 2021. URL https://api.semanticscholar.org/CorpusID:246705934.

R. B. Cleveland and W. S. Cleveland. Stl: A seasonal-trend decomposition procedure based on loess. *Journal of official statistics*, 6(1), 1990.

Wenjie Du, David Côté, and Yan Liu. Saits: Self-attention-based imputation for time series. *Expert Systems with Applications*, 219:119619, 2023.

Huatian Gong, Qing Peng, Linwei Liu, and Xiaoguang Yang. A decision-making system for traffic management during large-scale road network construction. *Expert Systems with Applications*, 292:128527, 2025. ISSN 0957-4174. doi: https://doi.org/10.1016/j.eswa.2025.128527. URL https://www.sciencedirect.com/science/article/pii/S0957417425021463.

Xiao Han, Saima Absar, Lu Zhang, and Shuhan Yuan. Root cause analysis of anomalies in multivariate time series through granger causal discovery. In *The Thirteenth International Conference on Learning Representations*, 2025. URL https://openreview.net/forum?id=k38Th3x4d9.

Leonardo Hoinaski, Camilo Bastos Ribeiro, Robson Will, Marlon Brancher, Rafaela Chiminelli Borth, Fábio Castagna da Silva, Igor Vinicius Reynaldo Tibúrcio, Diogo Lopes, Taciana Toledo de Almeida Albuquerque, Rizzieri Pedruzzi, Neyval Costa Reis, Weeberb J. Réquia, and Maria de Fatima Andrade. A model-based framework for prioritizing emission controls in data-scarce regions: Insights from air quality management in santa catarina, brazil. *Journal of Cleaner Production*, 525:146506, 2025. ISSN 0959-6526. doi: https://doi.org/10.1016/j.jclepro.2025.146506. URL https://www.sciencedirect.com/science/article/pii/S0959652625018566.

Mohammad Rafid Ul Islam, Prasad Tadepalli, and Alan Fern. Self-attention-based diffusion model for time-series imputation in partial blackout scenarios. In *Proceedings of the AAAI Conference on Artificial Intelligence*, volume 39, pp. 17564–17572, 2025.

Sorena Jafarigorzin, Fleur C. Khalil, Lionel J. Khalil, and Jeanne A. Kaspard. Machine learning-based localized predictive modeling of household energy consumption in the netherlands. *Energy and Buildings*, pp. 116420, 2025. ISSN 0378-7788. doi: https://doi.org/10.1016/j.enbuild.2025.116420. URL https://www.sciencedirect.com/science/article/pii/S0378778825011508.

Mourad Khayati, Alberto Lerner, Zakhar Tymchenko, and Philippe Cudré-Mauroux. Mind the gap: an experimental evaluation of imputation of missing values techniques in time series. *Proc. VLDB Endow.*, 13(5):768–782, January 2020. ISSN 2150-8097. doi: 10.14778/3377369.3377383. URL https://doi.org/10.14778/3377369.3377383.

Bing Li, Jiandong Gao, Ling Zhang, Juyuan Yin, and Wenqiang Bai. Evaluation of signal phasing and timing plans for mixed traffic condition based on information entropy. *Case Studies on Transport Policy*, 22:101590, 2025. ISSN 2213-624X. doi: https://doi.org/10.1016/j.cstp.2025.101590. URL https://www.sciencedirect.com/science/article/pii/S2213624X25002275.

Wei Liang, Yuhui Li, Kun Xie, Dafang Zhang, Kuan-Ching Li, Alireza Souri, and Keqin Li. Spatial-temporal aware inductive graph neural network for c-ITS data recovery. 24(8):8431–8442, 2023. ISSN 1558-0016. doi: 10.1109/TITS.2022.3156266. URL https://ieeexplore.ieee.org/abstract/document/9733959.

Zachary C Lipton, David Kale, and Randall Wetzel. Directly modeling missing data in sequences with rnns: Improved classification of clinical time series. In *Machine learning for healthcare conference*, pp. 253–270. PMLR, 2016.

Shuai Liu, Xiucheng Li, Yile Chen, Yue Jiang, and Gao Cong. Disentangling dynamics: Advanced, scalable and explainable imputation for multivariate time series. 37(7):4010–4022. ISSN 1558-2191. doi: 10.1109/TKDE.2025.3558405. URL https://ieeexplore.ieee.org/document/10949854.

SHUAI LIU, Xiucheng Li, Gao Cong, Yile Chen, and YUE JIANG. Multivariate time-series imputation with disentangled temporal representations. In *The Eleventh International Conference on Learning Representations*, 2023a. URL https://openreview.net/forum?id=rdjeCNUS6TG.

SHUAI LIU, Xiucheng Li, Gao Cong, Yile Chen, and YUE JIANG. Multivariate time-series imputation with disentangled temporal representations. In *The Eleventh International Conference on Learning Representations*, 2023b. URL https://openreview.net/forum?id=rdjeCNUS6TG.

Ivan Marisca, Andrea Cini, and Cesare Alippi. Learning to reconstruct missing data from spatiotemporal graphs with sparse observations. *Advances in neural information processing systems*, 35: 32069–32082, 2022.

Drilon Meha, Naser Sahiti, Bedri Dragusha, Rexhep Selimaj, and Jagruti Thakur. Empowering sustainable energy technologies for electricity production in kosovo using scenario approach analysis. *Sustainable Energy Technologies and Assessments*, 82:104504, 2025. ISSN 2213-1388. doi: https://doi.org/10.1016/j.seta.2025.104504. URL https://www.sciencedirect.com/science/article/pii/S2213138825003352.

Steffen Moritz and Thomas Bartz-Beielstein. imputets: time series missing value imputation in r. 2017.

Tong Nie, Guoyang Qin, Yunpeng Wang, and Jian Sun. Towards better traffic volume estimation: Jointly addressing the underdetermination and nonequilibrium problems with correlation-adaptive gnns. *Transportation Research Part C: Emerging Technologies*, 157:104402, 2023.

Tong Nie, Guoyang Qin, Wei Ma, Yuewen Mei, and Jian Sun. Imputeformer: Low rankness-induced transformers for generalizable spatiotemporal imputation. In *Proceedings of the 30th ACM SIGKDD Conference on Knowledge Discovery and Data Mining*, KDD '24, pp. 2260–2271, New York, NY, USA, 2024. Association for Computing Machinery. ISBN 9798400704901. doi: 10.1145/3637528.3671751. URL https://doi.org/10.1145/3637528.3671751.

Victor Garcia Satorras, Syama Sundar Rangapuram, and Tim Januschowski. Multivariate time series forecasting with latent graph inference, 2022. URL https://openreview.net/forum?id=JpNH4CW_zl.

Ashish Vaswani, Noam Shazeer, Niki Parmar, Jakob Uszkoreit, Llion Jones, Aidan N Gomez, Łukasz Kaiser, and Illia Polosukhin. Attention is all you need. *Advances in neural information processing systems*, 30, 2017.

Huiqiang Wang, Jian Peng, Feihu Huang, Jince Wang, Junhui Chen, and Yifei Xiao. MICN: MULTI-SCALE LOCAL AND GLOBAL CONTEXT MODELING FOR LONG-TERM SERIES FORECASTING. 2023.

Jianwei Wang, Ying Zhang, Kai Wang, Xuemin Lin, and Wenjie Zhang. Missing data imputation with uncertainty-driven network. *Proceedings of the ACM on Management of Data*, 2(3):1–25, 2024.

Jianwei Wang, Kai Wang, Ying Zhang, Wenjie Zhang, Xu Xiwei, and Xuemin Lin. On llm-enhanced mixed-type data imputation with high-order message passing. *Proceedings of the VLDB Endowment*, 18(10):3421 – 3434, 2025a.

Jun Wang, Wenjie Du, Yiyuan Yang, Linglong Qian, Wei Cao, Keli Zhang, Wenjia Wang, Yuxuan Liang, and Qingsong Wen. Deep learning for multivariate time series imputation: a survey. In *Proceedings of the Thirty-Fourth International Joint Conference on Artificial Intelligence*, IJCAI '25, 2025b. ISBN 978-1-956792-06-5. doi: 10.24963/ijcai.2025/1187. URL https://doi.org/10.24963/ijcai.2025/1187.

Yunshi Wen, Tengfei Ma, Ronny Luss, Debarun Bhattacharjya, Achille Fokoue, and Anak Agung Julius. Shedding light on time series classification using interpretability gated networks. In *The Thirteenth International Conference on Learning Representations*, 2025. URL https://openreview.net/forum?id=n34taxF0TC.

Haixu Wu, Jiehui Xu, Jianmin Wang, and Mingsheng Long. Autoformer: Decomposition transformers with auto-correlation for long-term series forecasting. *Advances in neural information processing systems*, 34:22419–22430, 2021.

Kejin Wu and Dimitris N Politis. Bootstrap prediction inference of nonlinear autoregressive models. *Journal of Time Series Analysis*, 45(5):800–822, 2024.

Zonghan Wu, Da Zheng, Shirui Pan, Quan Gan, Guodong Long, and George Karypis. Traversenet: Unifying space and time in message passing for traffic forecasting. *IEEE Transactions on Neural Networks and Learning Systems*, 35(2):2003–2013, 2024. doi: 10.1109/TNNLS.2022.3186103.

Jiayu Yang, Huabing Ke, Sunling Gong, Yaqiang Wang, Lei Zhang, Chunhong Zhou, Jingyue Mo, and Yan You. Enhanced forecasting and assessment of urban air quality by an automated machine learning system: The ai-air. *Earth and Space Science*, 12(1):e2024EA003942, 2025a. doi: https://doi.org/10.1029/2024EA003942. URL https://agupubs.onlinelibrary.wiley.com/doi/abs/10.1029/2024EA003942. e2024EA003942 2024EA003942.

Xinyu Yang, Yu Sun, Xinyang Chen, et al. Frequency-aware generative models for multivariate time series imputation. *Advances in Neural Information Processing Systems*, 37:52595–52623, 2024.

Xinyu Yang, Yu Sun, Xinyang Chen, Ying Zhang, and Xiaojie Yuan. Graph structure learning for spatial-temporal imputation: Adapting to node and feature scales. In Toby Walsh, Julie Shah, and Zico Kolter (eds.), *AAAI-25, Sponsored by the Association for the Advancement of Artificial Intelligence, February 25 - March 4, 2025, Philadelphia, PA, USA*, pp. 959–967. AAAI Press, 2025b. doi: 10.1609/AAAI.V39I1.32081. URL https://doi.org/10.1609/aaai.v39i1.32081.

Yongchao Ye, Shiyao Zhang, and James J. Q. Yu. Spatial-temporal traffic data imputation via graph attention convolutional network. In Igor Farkaš, Paolo Masulli, Sebastian Otte, and Stefan Wermter (eds.), *Artificial Neural Networks and Machine Learning – ICANN 2021*, pp. 241–252. Springer International Publishing, 2021. ISBN 978-3-030-86362-3. doi: 10.1007/978-3-030-86362-3_20.

Xiuwen Yi, Yu Zheng, Junbo Zhang, and Tianrui Li. St-mvl: Filling missing values in geo-sensory time series data. In *Proceedings of the 25th international joint conference on artificial intelligence*, 2016.

Jinsung Yoon, William R. Zame, and Mihaela van der Schaar. Estimating missing data in temporal data streams using multi-directional recurrent neural networks. 66(5):1477–1490, 2019. ISSN 1558-2531. doi: 10.1109/TBME.2018.2874712. URL https://ieeexplore.ieee.org/document/8485748.

Hsiang-Fu Yu, Nikhil Rao, and Inderjit S. Dhillon. Temporal regularized matrix factorization for high-dimensional time series prediction. In *Proceedings of the 30th International Conference on Neural Information Processing Systems*, NIPS'16, pp. 847–855, Red Hook, NY, USA, 2016. Curran Associates Inc. ISBN 9781510838819.

Ailing Zeng, Muxi Chen, Lei Zhang, and Qiang Xu. Are transformers effective for time series forecasting? In *Proceedings of the AAAI conference on artificial intelligence*, volume 37, pp. 11121–11128, 2023.

Tian Zhou, Ziqing Ma, Qingsong Wen, Xue Wang, Liang Sun, and Rong Jin. Fedformer: Frequency enhanced decomposed transformer for long-term series forecasting. In *International conference on machine learning*, pp. 27268–27286. PMLR, 2022.

A STATEMENTS AND PROOFS

A.1 PROOF FOR EQUIVALENCE IN TRAINING OBJECTIVES

With our modeling of the DGP in Section 2, we can prove that the following theorem holds:

Theorem 2 (Equivalence of model training target)**.** *With a DGP in the from of Section 2, model trained under objective:*

$$\min_{\mathcal{W}} \sum_{i\in[1,N],\tau\in[1,W]} \left[\mathrm{NN}\left(\{\mathbf{X}_{:,<\tau}\};\mathcal{W}\right)_i - \mathbf{X}_{i,\tau}\right]^2$$

is equivalent to training under objective:

$$\min_{\mathcal{W}} \sum_{i\in[1,N],\tau\in[1,W]} \left[\mathrm{NN}\left(\{\mathbf{X}_{:,<\tau}\};\mathcal{W}\right)_i - f(\mathbf{X}_{:,<\tau})_i\right]^2$$

Therefore, we can employ a prediction-subtraction-based approach to decompose signal and noise components of each timeseries. Note that the signal component here stands for the expected value of each measurement based on past information, or namely $f(\mathbf{X}_{:,<\tau})$, and noise represents the remaining exogenous shock disturbance.

Proof. Consider a model training process where we update parameters $\mathcal{W}$ through optimizing the objective function:

$$\min_{\mathcal{W}} \sum_{i\in[1,N],\tau\in[1,W]} \left[\mathrm{NN}\left(\{\mathbf{X}_{:,<\tau}\};\mathcal{W}\right)_i - \mathbf{X}_{i,\tau}\right]^2$$

Then, under the data generating process in Section 2, we substitute the iterative generating function into our objective:

$$\min_{\mathcal{W}} \sum_{i\in[1,N],\tau\in[1,W]} \left[\mathrm{NN}\left(\{\mathbf{X}_{:<\tau}\};\mathcal{W}\right)_i - f(\mathbf{X}_{:,<\tau})_i - \varepsilon_{i,\tau}\right]^2$$

Let $\nu_{i,\tau}(\mathcal{W}) := \mathrm{NN}\left(\{\mathbf{X}_{:,\tau}\};\mathcal{W}\right)_i - f(\mathbf{X}_{:,<\tau})_i$, we can expand and simplify the square terms as:

$$\min_{\mathcal{W}} \sum_{i\in[1,N],\tau\in[1,W]} \nu_{i,\tau}^2 - 2\nu_{i,\tau}\varepsilon_{i,\tau} + \varepsilon_{i,\tau}^2$$

Now, we analyze each component: 1) The target objective term $\sum \nu_{i,\tau}^2$; 2) the cross term $\sum -2\nu_{i,\tau}\varepsilon_{i,\tau}$; 3) A constant squared noise term $\sum \varepsilon_{i,\tau}^2$. The third term can be omitted for it is a constant against our parameters. As for the cross term, we compute:

$$\mathbb{E}\left[\frac{\partial}{\partial w}(-2\nu_{i,\tau}\varepsilon_{i,\tau})\right] = -2\mathbb{E}\left[\varepsilon_{i,\tau}\frac{\partial \nu_{i,\tau}}{\partial w}\right] = -2\mathbb{E}[\varepsilon_{i,\tau}]\mathbb{E}\left[\frac{\partial \nu_{i,\tau}}{\partial w}\right] = 0$$

which implies the expected gradient for the second term vanishes because noise is independent of all previous observations. Therefore, on the whole, the only term contributing a non-zero expected gradient to our objective function would be the first term. Effectively, we are optimizing on

$$\min_{\mathcal{W}} \sum_{i\in[1,N],\tau\in[1,W]} \left[\mathrm{NN}\left(\{\mathbf{X}_{:,<\tau}\};\mathcal{W}\right)_i - f(\mathbf{X}_{:,<\tau})_i\right]^2$$

Therefore, under the data generating process, the prediction-based decomposition can learn to fit on expected future signal though the optimization function contains noise. □

A.2 LIMITATION OF PRIOR SPATIAL-TEMPORAL INTERCONVERSION

Proof. In this section, we establish the superiority of our augmented bipartite graph framework against existing linear spatial-temporal transformation architecture by demonstrating that conventional linear spatial-temporal interconversion mechanisms and spatial interaction layers emerge as degenerated case of our general formulation.

Specifically, the M-RNN architecture and its SOTA derivatives (GRIN, GSLI, Imputeformer) employ interleaved spatial-temporal operations that correspond to a restricted parameterization of our signal component customization in Section 4.3.2 or noise component customization in Section 4.3.2. These constraints manifest in two primary forms:

1. **Structural Degeneracy**: By enforcing $\mathbf{E}^{\mathrm{S}}\mathbf{W}^{(l)}\mathbf{E}^{\mathrm{S},\top} = \mathbf{A}$ (where $\mathbf{A}$ denotes the given adjacency matrix from $\mathcal{G}^{\mathrm{S}}$), existing methods collapse our learnable bipartite projections to static graph representations.

2. **Form Restriction**: The sparse spatial transformer in Imputeformer (Nie et al., 2024) corresponds to a constrained instantiation of our propagation function for signal, where adaptive edge weights $\mathbf{W}^{(l)}$ are replaced by isolated attention matrices $\{\mathbf{Q}_h\mathbf{K}_h^\top\}_{h=1}^H$ with predefined sparsity patterns, where H denotes the number of attention heads.

The architectural degeneracy inherent in existing designs imposes strict constraints on their theoretical expressiveness, which mathematically guarantees inferior performance relative to our augmented bipartite graph framework under any learnable parameterization. □

A.3 Validity of DGP Assumptions

We adopt the assumption that the data-generating process (DGP) takes the form $\mathbf{X}_{i,\tau} = f(\mathbf{X}_{i,<\tau}) + \varepsilon_{i,\tau}$, where we refer to $f(\mathbf{X}_{:,<\tau})$ as the signal component, and to $\varepsilon_{i,\tau}$ as the noise component. We further impose three assumptions on the statistical properties of $\varepsilon_{i,\tau}$. Among these assumptions, the second assumption $\varepsilon_{i,\tau} \perp \varepsilon_{j,\omega}, \forall j \in \{1,\dots,N\}, \omega \neq \tau$ entails that the noise component lacks temporal dependency, may appear overly restrictive or insufficiently general. Therefore, in this section, we provide a mathematical justification to support the generality of this assumption.

Consider a DGP whose $\varepsilon_{i,t}$ does not satisfy the second assumption (i.e. it exhibits temporal dependencies). For clarity, we refer to its $f(\mathbf{X}_{i,<\tau})$ as the **trend** and to its $\varepsilon_{i,\tau}$ as the **shock**. Since shock exhibits temporal structures, it can be decomposed into a predictable component and an unpredictable remainder:

$$\varepsilon_{i,\tau} = g(\varepsilon_{:,<\tau}) + \nu_{i,\tau} \tag{17}$$

where $g(\cdot)$ is a non-linear autoregressive function describing the predictable expected exogenous shock component based on past **shock information**, and $\nu_{i,\tau}$ is the non-predictable component independent of **any previous information**. Moreover, since the exogenous shock $\varepsilon_{i,\tau} = \mathbf{X}_{i,\tau} - f(\mathbf{X}_{:,<\tau})$, it is itself a function of $\mathbf{X}_{:,\leq\tau}$. Hence, we can equivalently write:

$$\varepsilon_{i,\tau} = \tilde{g}(\mathbf{X}_{i,<\tau}) + \nu_{i,\tau} \tag{18}$$

where $\tilde{g}(\cdot)$ is a non-linear autoregressive function describing the predictable expected exogenous shock component based on past **observations**. Substituting this expression back to the original DGP yields

$$\mathbf{X}_{i,\tau} = f(\mathbf{X}_{i,<\tau}) + \tilde{g}(\mathbf{X}_{i,<\tau}) + \nu_{i,\tau} \tag{19}$$

since both $f(\cdot)$ and $\tilde{g}(\cdot)$ takes past observations as inputs, we can combine them into a single autoregressive function $h(\cdot)$:

$$\mathbf{X}_{i,\tau} = h(\mathbf{X}_{i,<\tau}) + \nu_{i,\tau} \tag{20}$$

where $h(\mathbf{X}_{i,<\tau}) := f(\mathbf{X}_{i,<\tau}) + \tilde{g}(\mathbf{X}_{i,<\tau})$; and $\nu_{i,\tau}$ is the previously defined non-predictable component independent from any previous information. We then define $h(\mathbf{X}_{i,<\tau})$ as the new **signal** and $\nu_{i,\tau}$ as the new **noise**. Under this reparameterization, the noise is, by construction, temporally independent of the past, thereby satisfying the three assumptions imposed on noise.

To further demonstrate and clarify these claims, we've also examined components decomposed by the model and compared against the original trend and shock, as well as DGP-defined signal and noise in Section D.2.

B Implementation Detail

B.1 Datasets

Air Quality Datasets **AQI** contains hourly PM2.5 measurements collected from 437 monitoring stations in Beijing from 2014/05/01 01:00:00 to 2015/04/30 23:00:00. We adopt the standard evaluation split following Yi et al. (2016); Cao et al. (2018), where data from March, June, September, and December is used for testing, and the remaining for training. Adjacency matrix for the exogenous spatial graph are constructed using geographical coordinates of each sensor as in Yi et al. (2016); Cao et al. (2018). And **AQI36** is a subset including the first 36 monitoring stations.

Name	N	T	C	Interval	Type
AQI	437	8760	1	1h	Air Quality
AQI36	36	8759	1	1h	Air Quality
METR-LA	207	34272	1	5min	Traffic
PEMS-BAY	325	52128	1	5min	Traffic
PEMS03	358	26208	1	5min	Traffic
PEMS04	307	16992	3	5min	Traffic
PEMS07	883	28224	1	5min	Traffic
PEMS08	170	17856	3	5min	Traffic
HAR	561	10299	1	1.28s	Healthcare
ETTm1	7	69680	1	15min	Smart Grid
ETTm2	7	69680	1	15min	Smart Grid
ELERGONE	370	105215	1	15min	Smart Grid

Table 2: Statistical Summary of Datasets

Traffic Datasets We adopt two subtypes of traffic datasets for testing. **METR-LA** and **PEMS-BAY** provide road speed data sampled every 5 minutes from sensors in Los Angeles and San Francisco Bay areas. **PEMS03**, **PEMS04**, **PEMS07**, and **PEMS08** consist of traffic volume data collected by Cal-trans Performance Measurement System (PeMS), also sampled at 5-minute intervals. For these, we construct adjacency matrix for the exogenous spatial graph according to the official highway networks.

Human Activity Recognition Dataset **HAR** (Human Activity Recognition) is a popular dataset consisting of sensor signals collected from wearable devices worn by volunteers as they perform various physical activities. The data are pre-processed to a sampling interval of 1.28 seconds and comprise 561 different sensors, including accelerometers and gyroscopes from different body locations. As the dataset does not provide explicit exogenous spatial graph, we construct a fully connected graph among all sensors to allow comprehensive modeling of sensor interactions. In addition to evaluating imputation error, **HAR** allows us to evaluate the imputation quality on downstream classification tasks, using activity labels provided for each sequence.

Smart Grid Dataset We adopt two subtypes of smart grid dataset for testing. **ETTm1** and **ETTm2** are two Electric Transformer Temperature dataset each comprising 7 sensor measurements, including load and oil temperature from an electrical transformer station. These datasets cover the period from 2016/07 to 2018/07 with a 15-minute sampling interval. **ELERGONE** contains electricity consumption records from 370 clients, sampled every 15 minutes from 2011 to 2014. For all these datasets, we follow the common data splitting protocol, allocating 10% of the data for validation and 20% for testing. As no exogenous spatial graphs are provided for these datasets, we adopt a fully connected adjacency matrix for models that require graph information.

B.2 Evaluation Metrics and Dataset Masking Strategy

We use both the RMSE and MAE for evaluation. The definition of MAE is as follows:

$$\text{MAE} = \frac{\sum_{i=1}^{N}\sum_{\tau=1}^{W}\mathbf{M}_{i,\tau}\cdot\left|\widehat{\mathbf{X}}_{i,\tau}-\mathbf{X}_{i,\tau}\right|}{\sum_{i=1}^{N}\sum_{\tau=1}^{W}\mathbf{M}_{i,\tau}} \tag{21}$$

The definition of RMSE is as follows:

$$\text{RMSE} = \sqrt{\frac{\sum_{i=1}^{N}\sum_{\tau=1}^{W}\mathbf{M}_{i,\tau}\cdot\left(\widehat{\mathbf{X}}_{i,\tau}-\mathbf{X}_{i,\tau}\right)^{2}}{\sum_{i=1}^{N}\sum_{\tau=1}^{W}\mathbf{M}_{i,\tau}}} \tag{22}$$

To ensure experimental consistency and fair benchmarking, we adopt data masking strategies similar to previous work (Nie et al., 2024; Cini et al., 2021). For **AQI** and **AQI36**, simulated sensor faults are generated following the original procedure in ST-MLV (Yi et al., 2016), where an observation is manually dropped if it isn't naturally missing and the observation from the same time last month is missing. For all other datasets, we evaluate both point missing and block missing scenarios, as commonly employed in (Cao et al., 2018; Cini et al., 2021; Nie et al., 2024):

1) Point missing: Missing values are sampled independently for each observation using a Bernoulli distribution $\mathbf{M}_{i,\tau} \sim \mathrm{B}(1, 0.25)$, where each observation is randomly masked with a probability of 25%. 2) Block missing: This scenario simulates more realistic sensor failures with continuous outages. First an initial mask $\mathbf{M}_1$ is generated using the same point-wise Bernoulli process as above but with a lower probability of 5%. Next, to mimic outages, a start mask $\mathbf{M}_2$ is created by sampling $\mathbf{M}_{2,i,\tau} \sim \mathrm{B}(1, 0.0015)$ for each sensor i and time step τ. Each activated failure represents a continuous outage of length $\mathbf{L}_{i,\tau} \sim \mathrm{Uniform}(12, 48)$. The final block missing mask is computed as the following equation:

$$\mathbf{M} = \mathbf{M}_1 \vee \mathrm{Span}(\mathbf{M}_2, \mathbf{L}) \tag{23}$$

where $\vee$ denotes the logical OR operation and $\mathrm{Span}(\cdot, \cdot)$ expands each selected outage starting point into a continuous missing block of the specified length. Since we train all our model under $\mathrm{seed} = 2$, all models share the same missing mask for each dataset under the same missing pattern.

For **AQI** and **AQI36**, we follow the original procedure in ST-MLV (Yi et al., 2016) and uses March, June, September and December as the testing set; 10% of the remaining adjacent but non-overlapping data-points preceding each testing month is used as the validation set; and the remaining non-overlapping data-points are used as the training set. For all other datasets, we follow previous works (Nie et al., 2024; Cini et al., 2021) and uses the beginning 70% data-points for training; the next non-overlapping 10% for validation and the final non-overlapping 20% for testing. The non-overlapping segmentation guarantees that none of the validation and testing set will be visible to the model during training.

During training, we randomly mask out an additional 10% if the non-missing observations to facilitate more rigid model training and avoid overfitting on specific missing patterns. See Section B.3 for the loss function used during training.

Following previous works Nie et al. (2024), for non-matrix factorization methods, we evaluate the model's out-of-sample (OOS) imputation performance, ensuring that no information from the validation or testing set is exposed to the model during training. For in-sample methods (i.e., TIDER, adaTIDER and LCR), we evaluate the mode's in-sample (IS) imputation performance, where only the ground-truth of dropped observations in testing and validation sets are not shown to the model during training.

B.3 Train Loss Design

To enable effective self-supervised learning, we adopt a dual-objective training strategy following previous work Du et al. (2023). The loss function combines observed reconstruction loss (ORL) and masked imputation loss (MIL) to ensure accurate reconstruction of missing values. Specifically, the loss functions are defined as:

$$l_{\mathrm{MIL}} = \frac{\sum_{i=1}^{N}\sum_{\tau=1}^{W}\left(1 - \mathbf{M}_{i,\tau}^{(t)}\right) \cdot \ell\left(\widehat{\mathbf{X}}_{i,\tau}, \mathbf{X}_{i,\tau}^{(t)}\right)}{\sum_{i=1}^{N}\sum_{\tau=1}^{W}\left(1 - \mathbf{M}_{i,\tau}^{(t)}\right)} \tag{24}$$

$$l_{\mathrm{ORL}} = \frac{\sum_{i=1}^{N}\sum_{\tau=1}^{W}\mathbf{M}_{i,\tau}^{(t)} \cdot \ell\left(\widehat{\mathbf{X}}_{i,\tau}, \mathbf{X}_{i,\tau}^{(t)}\right)}{\sum_{i=1}^{N}\sum_{\tau=1}^{W}\mathbf{M}_{i,\tau}^{(t)}} \tag{25}$$

where $\ell(\cdot, \cdot)$ represents element-wise reconstruction loss (e.g. mean absolute error). The overall training loss combines both components:

$$l = l_{MIL} + l_{ORL} \tag{26}$$

GraphTSI is updated by minimizing the final loss l.

C Additional Results

C.1 Benchmark RMSE results

Dataset	Mask	Avg.	GRIN	GSLI	BRITS	TIDER	adaTIDER	LCR	UnIMP	SAITS	Imputeformer	**GraphTSI**	
AQI36	Simulated	56.9312	22.0190	27.1960	23.1762	34.7269	77.0252	68.0342	34.5819	36.4735	27.1911	**19.3724**	-12.020%
AQI		67.2950	27.5155	29.3724	33.8573	48.8622	48.6232	51.4744	35.0683	36.1205	29.9331	**24.9411**	-9.356%
METR-LA	Point	22.2447	3.7283	3.5297	8.3640	13.7551	14.3426	13.4495	4.4427	6.9162	3.5208	**3.4367**	-2.389%
	Block	22.3203	5.9433	5.8599	8.9805	15.3985	13.5838	14.3068	7.2275	8.4585	6.0490	**5.7516**	-1.848%
PEMS-BAY	Point	9.3962	1.2245	1.1986	3.7387	6.4565	6.8333	7.5620	1.6796	3.0573	1.1591	**1.0761**	-7.163%
	Block	9.4969	2.4365	2.5574	3.7126	6.4292	6.7854	7.6067	3.2665	3.6806	2.4118	**2.2382**	-7.198%
PEMS03	Point	110.4516	14.6384	13.0551	26.0660	49.5692	53.4239	52.2824	17.1393	28.1297	13.3883	**11.5974**	-11.166%
	Block	110.5333	20.2423	15.8434	23.1337	45.3507	56.4151	47.0515	24.8856	26.1246	16.0300	**14.2961**	-9.766%
PEMS04	Point	74.6774	14.8118	8.8302	23.7165	34.4027	36.0054	36.2034	15.9019	21.6576	15.6002	**8.6081**	-2.515%
	Block	74.8785	23.0640	16.3150	22.9959	33.6004	34.3942	36.0808	19.0009	21.8728	17.7224	**14.8050**	-9.255%
PEMS07	Point	149.5555	20.0317	17.9646	44.5825	71.5680	73.2541	66.7169	26.9325	47.6898	18.7524	**17.8850**	-0.443%
	Block	149.9398	27.9339	**25.8423**	45.0385	69.8824	73.2640	67.3023	34.4643	48.9659	27.9847	25.8727	+0.118%
PEMS08	Point	65.4021	10.9649	6.3271	21.9158	30.3188	33.2092	28.8825	11.9393	17.8621	11.1520	**5.9480**	-5.992%
	Block	66.1944	19.9088	13.8394	20.4427	29.7691	17.3010	32.4780	28.8512	18.6814	13.1710	**12.0533**	-8.486%
HAR	Point	0.3237	D.N.F.	0.0719	0.1058	0.2341	0.2010	0.2469	0.1205	0.1105	0.0781	**0.0679**	-5.550%
	Block	0.3162	D.N.F.	0.0800	0.0946	0.1949	0.1321	0.1973	0.2414	0.1061	0.0752	**0.0668**	-11.260%
ETTm1	Point	5.9672	0.7907	0.4685	0.5749	4.3586	3.6917	5.4398	D.N.F.	0.4805	0.4779	**0.4469**	-4.610%
	Block	6.0152	D.N.F.	1.1718	1.4275	4.3706	3.7317	5.5418	D.N.F.	**0.9531**	1.3146	1.0806	+13.373%
ETTm2	Point	8.4321	D.N.F.	0.5602	1.1929	5.3972	4.4453	7.2473	D.N.F.	0.6114	0.6067	**0.4892**	-12.674%
	Block	8.2934	D.N.F.	1.5953	2.3899	5.3795	4.3477	7.0941	D.N.F.	1.3585	2.0353	**1.2853**	-5.388%
Elergone	Point	2244.2345	D.N.F.	**305.0960**	628.0602	1467.8114	1557.9351	1540.4912	D.N.F.	567.2914	320.9664	335.6993	+10.031%
	Block	2162.3831	D.N.F.	489.3702	613.5619	1345.2236	1431.5295	1378.5088	D.N.F.	522.3876	413.4545	**408.0314**	-1.312%
Average Improvement		-82.671%	-21.821%	-8.915%	-43.408%	-70.273%	-72.066%	-73.064%	-34.896%	-37.725%	-14.609%	—	

Table 3: RMSE Performance of models. The final column shows average performance gain over each benchmark setup, and the final row shows average performance gain over each model. D.N.F. indicates not finished within 8 hours for ETTm1, ETTm2 and Elergone datasets and not finished within 48 hours for other datasets.

In this experiment, we report the imputation performance of different methods on multivariate time series data using RMSE. The results are summarized in Table 3, covering 9 datasets and different masking strategies. As shown in the table, transformer-based approaches such as Imputerformer and graph-based method GSLI, achieve competitive performance on the evaluated datasets. Moreover, our proposed method, GraphTSI, consistently achieves the best or second-best RMSE across almost all datasets. Notably, GraphTSI achieves an average RMSE improvement of 15.260% over Imputerformer and 9.064% over GSLI. These results highlight the effectiveness of GraphTSI for accurate time series imputation.

C.2 Additional Results for Missing Rates

To further examine the robustness of different methods, we evaluate imputation performance on METR-LA and PEMS-BAY under different missing rates. We include Imputeformer and GSLI as baseline since their outstanding performance in previous experiments. The results are shown in Figure 7. On both METR-LA and PEMS-BAY datasets, the MAE values increase steadily as the missing rate rises from 25% to 95%. Overall, GraphTSI consistently achieves the lowest error across all missing rates, demonstrating strong robustness even in extremely sparse conditions.

C.3 Additional Results for Window Sizes

To further evaluate the impact of window sizes on different methods, we investigate imputation performance on METR-LA and PEMS-BAY under varying window sizes. We include Imputeformer and GSLI as baselines due to their competitive performance in previous experiments. The results are presented in Figure 8. On both datasets, increasing the window size generally leads to improved accuracy for all methods. However, for extremely long window sizes ($W > 36$), the increasing window size provide marginal improvement, and performance slowly degrades due to larger variances created by smaller batch sizes. Notably, GraphTSI consistently achieves the lowest RMSE across all window sizes, highlighting its stability and effectiveness in capturing temporal dependencies under different temporal contexts.

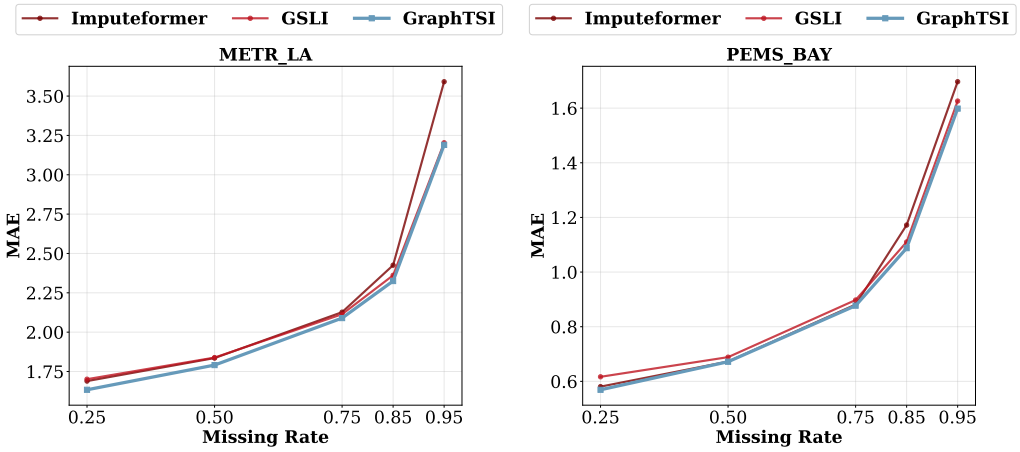

Figure 7: Results of different missing rate on METR-LA and PEMS-BAY datasets.

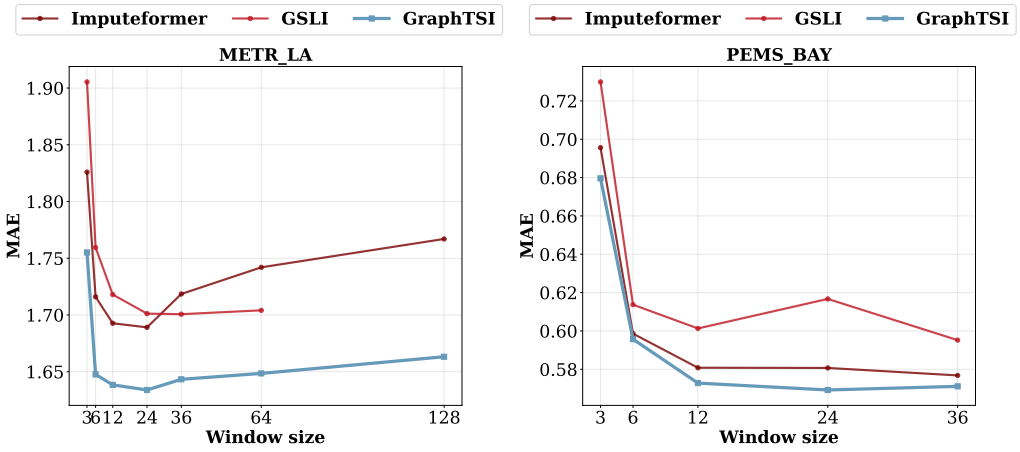

Figure 8: Result of different window sizes on METR-LA and PEMS-BAY datasets.

C.4 Additional Results for Different Missing Patterns

In this section, we examine model performance under extreme missing patterns in PEMS08 dataset. We include Imputeformer and GSLI as baselines due to their competitive performance in previous experiments. Following prior works (Khayati et al., 2020), we tested model performance on the following missing patterns: 1) **Overlap**: Block missing overlaps with each other, meaning at least one sensor fails at every time step; 2) **Blackout**: Block missing happens unanimously across all sensors; 3) **Sensor Failure**: One of the sensors fails throughout the entire test set. The results are presented in Table 4. These results demonstrated that GraphTSI consistently outperforms strong baselines across all extreme missingness scenarios. Notably, under Blackout—when all sensors are missing concurrently, GraphTSI reduces MAE by 53.44% relative to the best baseline, indicating robust cross-sensor and temporal interpolation. In Overlap and Sensor Failure settings, GraphT-

Missing Pattern	GSLI	Imputeformer	**GraphTSI**	
Overlap	7.7746	6.8932	**6.6936**	**-2.8956%**
Blackout	38.1689	29.1509	**13.5714**	**-53.4443%**
Sensor Failure	10.6389	10.1796	**9.3771**	**-7.8834%**

Table 4: MAE performance of models under different missing patterns.

SIachieves 2.90% and 7.88% relative MAE reductions, respectively, suggesting that the method remains effective when missing blocks are pervasive or when a single sensor is entirely absent.

D Case Study

D.1 Temporal Attention for Long Window

In this section, we demonstrate the attention matrix of the forward bi-unidirectional predictor to demonstrate the locality of attention spans in imputation tasks. Results are shown in Figure 9.

Of these attention heads, we can identify three primary patterns: 1) the third head in the first layer aggregates information from the beginning of each series; 2) the second head in the first layer and the fourth head in the third layer exhibit a pronounced periodic structure that decays gradually with increasing lag; 3) the remaining heads display strong locality, focusing predominantly on a narrow temporal window preceding each time step.

These results help explain the marginal gains in imputation accuracy observed for extremely long window sizes. They also highlight opportunities for future work through discrete transformers that reduce computation time with minimal impact on performance.

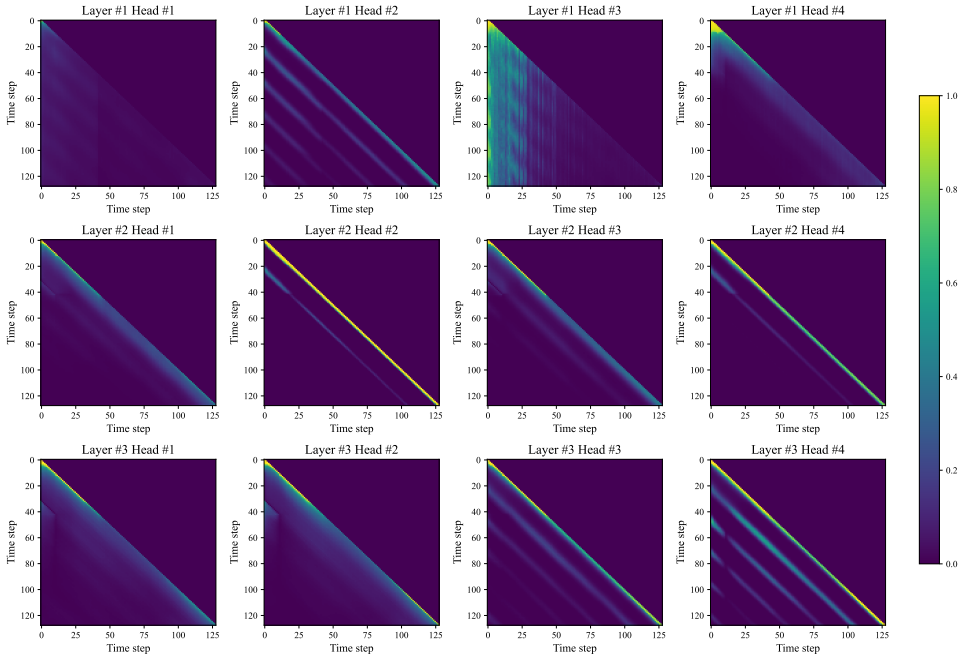

Figure 9: Attention matrices across all heads and layers of GraphTSI, evaluated on the METR-LA dataset. Each entry is aggregated as the 99th percentile over the batch and sensor dimension.

D.2 Separation of Signal and Noise

In this section, we examine the behavior of our model when exogenous shock exhibit temporal autocorrelation, as described in Section A.3, using an artificially generated dataset. First, we will establish the experiment setup; Next, we calculate the theoretical value of **trend** and **shock** based on the setup, as well as the theoretical value of **signal** and **noise** based on the DGP; Finally, we demonstrate the actual component decomposed and imputed by our model and compare them against each of the two pairs to provide empirical proof for the validity of our assumptions and the explainability of our model.

To construct the artificial dataset, we set the number of channels to $C = 1$ and construct each measurement from series i and time step τ as follows:

$$\mathbf{X}_{i,\tau} := \sin(\phi_i + \omega\tau) + \varepsilon_{i,\tau} \tag{27}$$

where ϕ_i is the initial phase of the sinusoidal trend; ω is the frequency; $\sin(\phi_i + \omega\tau)$ represents the entire sinusoidal trend; and $\varepsilon_{i,\tau}$ represents the exogenous shock defined as a Moving Average process:

$$\varepsilon_{i,\tau} = \sum_{\Delta=0}^{l-1} \nu_{i,\tau-\Delta} \tag{28}$$

where l is the lag of this $\mathrm{MA}(l)$ process, and $\nu_{i,\tau}$ is the underlying multivariate normally-distributed noise with zero mean and covariance matrix Σ:

$$\nu_{:,\tau} \sim \mathrm{N}(\mathbf{0}, \Sigma) \tag{29}$$

Under this setup, the sinusoidal **trend** is defined as $\sin(\phi_i + \omega\tau)$, and the exogenous **shock** is defined as $\varepsilon_{i,t}$. However, according to our DGP, the signal component should describe the predictable expected observation based on past information. Here, the sinusoidal trend via averaging through the past; the exogenous shock is partially predictable through a linear combination of $\varepsilon_{:,t-1}$, and $\varepsilon_{\neq i,t}$. Therefore, by definition, the target of **signal** should be $\mathbf{X}_{i,\tau} - \nu_{i,\tau}$, and the target of **noise** should be $\nu_{i,\tau}$. To test these claims, we build datasets with $N = 3, W = 24, C = 1, l = 9, \phi_i = 2i\pi/3, \omega = 2\pi/96$ and the covariance matrix as

$$\Sigma = \begin{pmatrix} 1 & 0.5 & 0.5 \\ 0.5 & 1 & 0.5 \\ 0.5 & 0.5 & 1 \end{pmatrix}$$

We employ the standard point-dropping mechanism to train and evaluate our model. The output hidden states of the bi-unidirectional predictors from both sides are passed through the MLP readout to retrieve our decomposed signal component, and the noise component is defined as the difference between our final imputation and the decomposed signal. Results are shown in Figure 10 and Figure 11. As we can clearly see, our decomposed signal component resembles more to the ground truth signal target, which is defined as $\mathbf{X}_{i,\tau} - \nu_{i,\tau}$, and the noise component resembles more to the one-period cross-sectional noise $\nu_{i,\tau}$ rather than the temporally correlated shock.

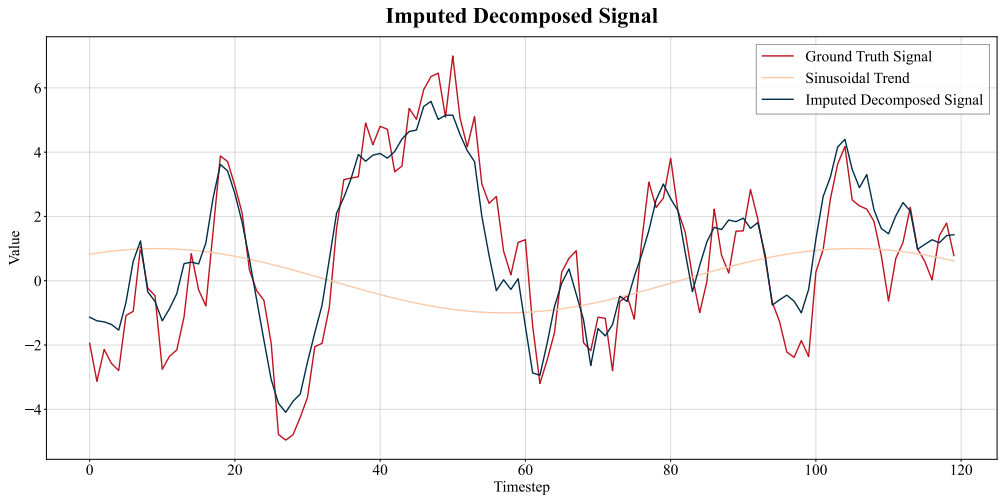

Figure 10: Decomposed signal component compared against sinusoidal trend and DGP-defined signal component

LLM USAGE

To enhance clarity and readability, we use Large Language Models (LLMs) as a general-purpose writing assistant for polishing. Specifically, after drafting the manuscript ourselves, we use LLMs

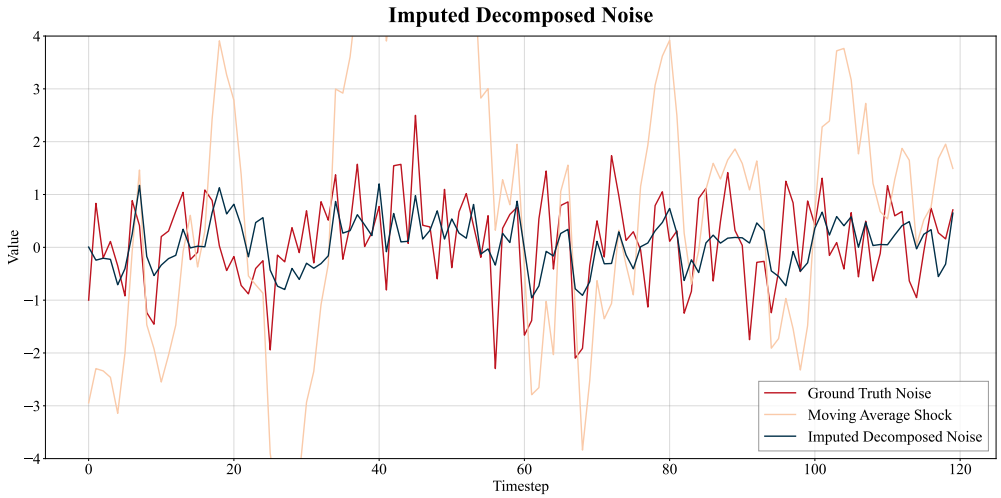

Figure 11: Decomposed noise component compared against exogenous moving average shock and DGP-defined noise component

to: 1) Suggest alternative phrasing to avoid repetitiveness while being consistent; 2) Check for consistency in tense, notation and other grammatical issues; 3) Asking for more standard terminology or abbreviations. We have reviewed and edited all LLM-generated text to ensure accuracy and faithfulness, and no text was incorporated without verification from authors.

The LLMs are NOT used for research ideation, experiment design or data analysis. All technical claims, equations, proofs, and conclusions are written and verified by the authors. We take responsibility for the content of this paper.